Nonlinear Optical and Photocurrent Responses in Janus MoSSe Monolayer and MoS_2-MoSSe Van der Waals Heterostructure

Alex Strasser[a,†], Hua Wang[a,†], and Xiaofeng Qian[a, b, *]

AUTHOR ADDRESS:

[a] Department of Materials Science and Engineering, Texas A&M University, College Station, TX 77843, USA

[b] Department of Electrical and Computer Engineering, Texas A&M University, College Station, TX 77843, USA

* E-mail: feng@tamu.edu

† These authors contributed equally to the work.

KEYWORDS: Janus 2D Materials; Circular Photocurrent; Shift Photocurrent; Second Harmonic Generation; First-Principles Calculations.

ABSTRACT

Two-dimensional (2D) transition metal dichalcogenides are a promising materials platform for a variety of optoelectronic device applications. Janus 2D materials are a rising class of 2D materials with low symmetry, which leads to the emergence of the out-of-plane electric polarization and piezoelectricity. Using first-principles density functional theory, we show that monolayer and bilayer heterostructure Janus MoSSe exhibit strong nonlinear optical responses that are vanishing in non-Janus form. The absence of horizontal mirror plane symmetry enables circular photocurrent as well as large out-of-plane second harmonic generation (SHG) and shift photocurrent. Through a comparative study of the Janus heterostructure MoS_2-MoSSe on five distinct stacking configurations, we find the magnitude of the out-of-plane SHG in the Janus heterostructure is enhanced due to interlayer coupling and interference effect compared to monolayer MoSSe. Thus, Janus 2D materials offer a unique opportunity for exploring nonlinear optical phenomena and designing configurable layered nonlinear optical materials.

Janus 2D transition metal dichalcogenides (TMDCs) represent a distinct new class of 2D materials whose crystalline symmetry and physical properties can be tailored via compositional engineering of 2D atomic layers in Janus MoSSe[1, 2] and other Janus structures.[3-7] The Janus structure naturally breaks the symmetry of the parent phase and facilitates charge transfer, which with promising applications in valleytronics,[8] water-splitting photocatalysis,[9] advanced optical devices,[10] etc.

Janus structuring, where one out of two symmetrical crystal planes of atoms is replaced with a crystal plane of different elements, naturally breaks the mirror and/or inversion symmetry of the parent phase and facilitates charge transfer, resulting in the out-of-plane dipole moment with several nontrivial physical consequences. First, it leads to large spin and valley splittings[11] with enhanced spin Hall conductivities[12] and strong piezoelectric response.[5, 13, 14] In addition, this dipole allows to achieve Ohmic contact with various metals.[15] In particular, interlayer coupling can be enhanced by the interlayer dipole-dipole interaction.[16] Very recently, monolayer lateral multi-heterostructures of MoS_2-MoSSe-MoSeS-$MoSe_2$ has been experimentally realized via room-temperature atomic-layer substitution, offering tremendous opportunity for artificial 2D superlattices of Janus 2D materials.[17]

Symmetry breaking upon Janus structuring also has a significant impact on linear and nonlinear optical (NLO) responses of 2D materials. The built-in dipole moment increases the separation of electron and hole wavefunctions and strengthens electron-phonon interaction, thereby inducing longer exciton radiative recombination lifetime.[18] Moreover, broken inversion symmetry in 2D Janus materials leads to the out-of-plane second harmonic generation (SHG),[19] and enables other even-order responses such as shift current and circular (injection) current,[20, 21]

bulk photovoltaic effect (BPVE),[22, 23] nonlinear anomalous Hall effect,[24-27] and interlayer sliding induced ferroelectric nonlinear anomalous Hall effect.[28, 29]

Here, we employ first-principles electronic structure theory to investigate NLO properties of monolayer Janus MoSSe and the vdW heterostructure of monolayer MoSSe and monolayer MoS_2. We find that both show strong SHG and second-order nonlinear shift and circular photocurrent responses. Additionally, the *k*-point resolved optical absorption and shift vector reveal the microscopic origin of shift current in Janus MoSSe. Our results suggest that Janus 2D materials and their vdW heterostructures provide unpreceded opportunities to unlock and enhance NLO responses of their parent pristine 2D materials, which may ultimately benefit the development of ultrathin NLO materials and novel Berry curvature dipole and shift dipole based nonlinear quantum memory.[28, 29]

Janus 2D transition metal dichalcogenides often have a chemical formula of MXY, where M is a transition metal (e.g. Mo, W) and X and Y are chalcogenides (S, Se, Te). The crystal and band structure is shown in Figure 1a. We optimized the lattice constants and atomic positions using first-principles density functional theory (DFT)[30, 31] with generalized gradient approximation in the Perdew-Burke-Ernzerhof (PBE) form.[32] Calculation details can be found in Methods section. For Janus MoSSe, the optimized lattice constant is 3.25 Å with the Mo-Se bond length of 2.53 Å and the Mo-S bond length of 2.42 Å, in agreement with the experimental results (3.22 Å, 2.58 Å, and 2.41 Å, respectively).[1] The difference in bond lengths of Mo-S and Mo-Se and the different chemical elements of S vs Se, highlighted in Figure 1b, are clear indicators of broken horizontal mirror symmetry, which gives rise to an out-of-plane dipole. Electronic band structure is shown in Figure 1c, which is calculated by DFT with spin-orbit coupling taken into

account. It shows a direct band gap of 1.47 eV at K, and the degeneracy was lifted at K due to the inversion symmetry breaking in Janus MoSSe.

Next, we carry out a group theoretical analysis to have a qualitative assessment of NLO responses, including SHG, shift current, and circular photocurrent.[21] The point group of monolayer Janus MoSSe is C_{3v}, one of the 11 noncentrosymmetric point groups. The 2nd order susceptibility represents the coefficient of the 2nd term of the Taylor expansion of the polarization equation, $P_a(2\omega) = \chi^{(2)}_{abc}(2\omega;\omega,\omega)E_b(\omega)E_c(\omega)$ where Einstein summation is assumed. P_a is the electric polarization along direction a induced by external field E_b and E_c at frequency ω. Both P and E are polar vectors, thus transform as $\Gamma_P=\Gamma_E=E+A_1$ in the C_{3v} point group. In order to obtain the representation of the 2nd order susceptibility, we shall take the direct product of the representations of the constituents (P_a, E_b, and E_c). For example, $\Gamma_P \otimes \Gamma_E = 2A_1 + A_2 + 3E$, which gives the representations of linear susceptibility $\chi^{(1)}_{ab}$ with two independent nonvanishing tensor elements due to the two totally symmetric representations (A_1). For second order NLO tensors, such as SHG, the corresponding representation is given by the product $\Gamma_P\otimes\Gamma_E\otimes\Gamma_E$. However, due to the permutation symmetry of two electric field $E_b(\omega)$ and $E_c(\omega)$, the direct product of $\Gamma_P\otimes\Gamma_E\otimes\Gamma_E$ contains the representations of all the tensor elements whether they are dependent or independent. So to obtain the representations of the independent elements, we follow Dresselhaus[33] by splitting the product of $\Gamma_E\otimes\Gamma_E$ (which is same as $\Gamma_P\otimes\Gamma_E$ due to the fact that both P and E are polar vectors readily identified by x, y, and z basis functions) into symmetric (Γ_s) and antisymmetric (Γ_a) portions upon permutation, $\Gamma_s = 2A_1 + 2E$ and $\Gamma_a = A_2 + E$. Γ_a are identified by R_x, R_y and R_z basis functions which are antisymmetric upon permutation of two indices in x, y, and z. To obtain the independent nonvanishing elements of the 2nd order NLO tensor, we discard antisymmetric portion to account for the intrinsic permutation symmetry

of $E_b(\omega)E_c(\omega)$, and compute the direct product of the symmetric portion ($\Gamma_s = 2A_1 + 2E$) and the second electric field (Γ_E): $\Gamma_P \otimes \Gamma_{EE} = \Gamma_P \otimes \Gamma_E \otimes \Gamma_E = \Gamma_s \otimes \Gamma_E = 4A_1 + 2A_2 + 6E$. The four totally symmetric representations (A_1) suggests that both SHG and shift current should have four independent tensor elements. In summary, Janus MoSSe with the C_{3v} point group symmetry shall have four independent nonzero tensor elements in their SHG and SC susceptibility tensor.

For circular photocurrent (CC), incident light is either left or right circularly polarized. For the 2nd order response under circularly polarized light, $\Gamma_C = \Gamma_E \otimes \Gamma_{E^*}$ transforms as R_j, there for $\Gamma_C = \Gamma_E \otimes \Gamma_{E^*} = E + A_2$ Therefore, $\Gamma_P \otimes \Gamma_C = (E + A_1) \otimes (E + A_2) = A_1 + 2A_2 + 3E$, indicating one *independent* nonzero linear optical tensor element. Effectively, this corresponds to carry out all possible combinations of the direct product $i \otimes R_j$, resulting in four nonzero elements from $(x, y) \otimes (R_x, R_y) = E^2 = A_1 + A_2 + E$, but only one *independent* element as they are all dependent. z transforms as A_1 and none of $R_i \otimes A_1$ will produce any total symmetric A_1 representation, therefore, neither circular photocurrent along z can be observed ($z \otimes R_x = z \otimes R_y = E$), nor circular photocurrent along x or y when circularly polarized light propagates along z ($x \otimes R_z = y \otimes R_z = E$). Therefore, our analysis predicts one independent and four nonzero tensor elements for circular photocurrent in Janus MoSSe with C_{3v} point group.

The SHG susceptibility $\chi^{(2)}$, shift current susceptibility $\sigma^{(2)}$, circular photocurrent (injection current) $\eta^{(2)}$, and polarization anisotropy of monolayer Janus MoSSe were calculated with spin-orbit coupling taken into account, and the results are shown in Figure 2. Figure 2a shows the electric field alignment with the lattice. Figure 2b shows the polarization anisotropy, which exhibits C_{3v} symmetry, as expected, with a large maximum $|\chi^{(2)}_{yxx}|$ of 5.6×10^5 pm^2/V at 3.0 eV, larger than MoS_2 (3.02×10^5 pm^2/V at 1.67 eV) and an order of magnitude larger than h-BN.[34]

Figure 2d shows the magnitude of the SHG, showing $\chi^{(2)}_{yxx}$ has high SHG at the static limit, 9×10^4 pm^2/V, whereas the rest of the non-equivalent tensor elements showed SHG at the static limit of $<10^4$ pm^2/V. We see 11 tensor elements plotted here, with four independent elements, as expected. Unlike in MoS_2, $\chi^{(2)}_{zxx}$, $\chi^{(2)}_{zyy}$, $\chi^{(2)}_{zzz}$, as well as $\sigma^{(2)}_{zxx}$, $\sigma^{(2)}_{zyy}$, and $\sigma^{(2)}_{zzz}$ are all nonzero. Interestingly, while $\chi^{(2)}_{yxx}$ and $\sigma^{(2)}_{yxx}$ is the strongest nonlinear response, the second largest direction of photoresponse is in the z-direction, corresponding to $\chi^{(2)}_{zxx}$, $\chi^{(2)}_{zyy}$, $\sigma^{(2)}_{zxx}$, and $\sigma^{(2)}_{zyy}$. The largest shift current elements, $\sigma^{(2)}_{yxx}$ and $\sigma^{(2)}_{zxx}$, both have their biggest response in the 2-3.5 eV range, with some peak alignment, particularly at 2.91 eV (see Figure 2e). The smaller tensor elements, $\sigma^{(2)}_{xxz}$ and $\sigma^{(2)}_{zzz}$, get more active at the higher energy photons above 4 eV. The significance of the result lies in the breaking of the horizontal mirror plane in the Janus structure resulting in new directions of SHG and shift current (SC), as well as the presence of significant circular photocurrent (shown in Figure 2c) that does not exist in MoS_2 or other D_{6h} materials. Both SHG and SC are present and large in the out-of-plane direction, including zxx, zyy, and zzz, which opens up new applications in shift current photovoltaics and other optoelectronics.[23, 35]

Spin-orbit coupling has some slight effect on NLO responses, including some magnitude reduction at ~1.5 eV for $\chi^{(2)}_{yxx}$ and ~3.4 eV for $\chi^{(2)}_{zzz}$ (see Figure S1), because it splits the electronic bands and changes the resonances embedded in the denominators of NLO susceptibility tensors. Furthermore, a scissor operator of 0.28 eV to correct the original band gap (1.47 eV) of Janus monolayer MoSSe from our DFT calculations to 1.75 eV, and the results in Figure S2 show the resulting horizontal shift with nearly negligible magnitude reduction across the entire frequency range of 0-6 eV.

Figure 3 shows the shift current as a function of frequency for Janus SMoSe and SeMoS. These two Janus structures differ by swapping the S and Se atoms on the top and bottom atomic layer, which switches the chirality of the two structures. The results show that the sign of the shift current is exactly reversed, while the magnitude remains the same. The shift current is reversed because the shift vector changes sign when the chirality is switched. Therefore, stacking-dependent chirality can potentially be utilized to design 2D materials and their van der Waals heterostructures with tailored NLO responses, such as gyrotropic order by design.[36] As the experimental apparatus improves, chirality has potential to be switched *in situ* through rotation or atomic replacement, granting an additional degree of freedom in optoelectronic devices.

To understand the microscopic origin of the NLO responses of Janus monolayer SMoSe, we calculated several *k*-resolved physical quantities including absorption, shift vector, and shift current, as shown in Figure 4. The Figure 4a-d displays the optical absorption strength for x-polarized light, $r^x_{nm} r^x_{mn}$. Figure 4a-c show absorption divided by photon energy, 1.5, 2.0, and 2.5 eV, respectively, whereas Figure 4d shows absorption for all energy values. Close to the calculated bandgap (1.47 eV), absorption is exclusively at and around the high symmetry points in the Brillouin zone, namely K and K'. As the incident photon energy increases, the absorption in reciprocal space disperses out from the high symmetry k-points, centered around the valleys K and K', but the absorption remains minimal around the Γ-point, which can also be seen in Figure 4d. Figure 4e displays the shift vector, which approaches 10 Å around the high symmetry points, greater than the lattice parameter. The shift vector is given by $R^{a,b}_{nm}(\boldsymbol{k}) = -\frac{\partial \phi^b_{nm}(\boldsymbol{k})}{\partial k^a} + \mathcal{A}^a_n(\boldsymbol{k}) - \mathcal{A}^a_m(\boldsymbol{k})$, where $\phi^b_{nm}(\boldsymbol{k})$ is the phase factor of the interband Berry connection $\boldsymbol{r_{nm}}(\boldsymbol{k}) = |\boldsymbol{r_{nm}}(\boldsymbol{k})| e^{i\phi_{nm}(\boldsymbol{k})}$ and $\boldsymbol{\mathcal{A}_n}(\boldsymbol{k}) = i\langle n|\nabla_{\boldsymbol{k}}|n\rangle$ is the intraband Berry connection. The interband Berry connection is given by $\boldsymbol{r}_{nm} = i\langle n|\nabla_{\boldsymbol{k}}|m\rangle$. As discussed elsewhere,[21] the shift vector can

be calculated from the optical absorption and shift current by $R_{nm}^{a,b}(\boldsymbol{k}) = \frac{Im[r_{nm}^{b} r_{nm;k^a}^{b}]}{|r_{nm}^{b}|^2}$, removing divergences at the optical zero points during summation. Figure 4f displays the k-resolved shift current strength for monolayer Janus MoSSe, which shows the strongest positive value around the high symmetry k-points and a strong negative value around the optical zero points. The shift current result looks qualitatively similar to the shift vector (except the removed divergences). The results also demonstrate a direction shift in points nearby the K and K' points, where a positive shift current is almost halfway encircled by a negative shift current in a symmetrical fashion, with the location of the positive and negative currents flipping with valley index (K vs K'). Thus, shift current in Janus MoSSe is a valley-dependent phenomenon displaying the symmetries of the material, as seen in Figure 4e-f. The valley dependence arises from the presence of time-reversal symmetry, ensuring identical magnitude but opposite sign of the Berry curvature at the K and K' valleys, while the sum of shift vector in the first Brillouin zone vanishes. This valley dependent nonlinear photocurrent can be probed by breaking time-reversal symmetry, such as by applying magnetic field or under circularly polarized light, resulting in the circular photocurrent seen in Figure 2c that arises from the nonzero Berry curvature dipole.

Inversion symmetry breaking guarantees finite even-order nonlinear optical responses of materials in their corresponding tensor elements; however, the strength of the corresponding responses depends on several factors. Using shift current susceptibility tensor $\sigma^{abc}(0;\ \omega, -\omega)$ as an example,

$$\sigma^{abb}(0;\ \omega, -\omega) = -\frac{\pi e^3}{2\hbar^2} \int [d\boldsymbol{k}] \sum_{nm\boldsymbol{\sigma}} f_{nm} R_{nm}^{a,b}(\boldsymbol{k})\, r_{nm}^{b} r_{mn}^{b} \delta(\omega_{mn} - \omega)$$

where $f_{nm} \equiv f_n - f_m$ and f is the Fermi-Dirac distribution and $[d\boldsymbol{k}] \equiv \frac{d\boldsymbol{k}}{(2\pi)^d}$ and $d \equiv$ number of dimensions. So, materials with large transition matrix element $r^b_{nm} r^b_{mn}$ (or, strong interband dipole moment), large shift vector $R^{a,b}_{nm}(k)$, as well as large joint density of states can potentially have strong nonlinear shift current responses. However, shift vector can have positive and negative signs at different regions of Brillouin zone, hence strong cancellation needs to be avoided. Furthermore, circular (injection) current η^{abc} is described for light propagating in the z-direction by

$$\eta^{a,z}(0;\omega,-\omega) = \frac{i\pi e^3}{2\hbar^2}\int [d\boldsymbol{k}] \sum_{nm\boldsymbol{\sigma}} f_{nm}\Delta^a_{nm}\Omega^z_{mn}(\boldsymbol{k})\delta(\omega_{mn}-\omega)$$

where $\Omega^z_{mn}(\boldsymbol{k}) \equiv i\left[r^x_{mn}, r^y_{nm}\right] = -i\left[r^y_{mn}, r^x_{nm}\right]$ is the local Berry curvature between bands m and n, and $\hbar\Delta^a_{mn} \equiv v^a_{mm} - v^a_{nn}$ is the group velocity difference in bands m and n. Thus, materials with strong Berry curvature, large group velocity difference, and high joint density of states may potentially have large circular photocurrent. Similar to the case of shift current, for circular photocurrent the Berry curvature and the group velocity difference can have different signs in different regions of Brillouin zone, thus strong cancellation also needs to be avoided.

As van der Waals stacking can be precisely controlled in experiment, we also investigated bilayer vdW heterostructures made of MoS_2 and MoSSe with five different stacking configurations, including AA, AA', AB, A'B, and AB'. The point group of all five MoSSe-MoS_2 heterostructures is C_{3v}. The configurations for MoSSe-MoS_2 heterostructure are shown in Figure S3 and the naming nomenclature and relations between the configurations for bilayer MoS_2 are detailed in Table S1 in Supporting Information. In principle, it is possible to introduce another variation by swapping the S and Se atoms and forming two different bilayer vdW heterostructures with the same stacking configuration but a distinct chirality. Here we focus on

the SMoS-SMoSe heterostructure in this work, as this heterostructure can be achieved in experiment by replacing the S atoms on the top MoS_2 layers by Se that are adjacent to the bottom MoS_2 layer.

Figure 5 shows the calculated SHG susceptibility $\chi^{(2)}$ and shift current susceptibility $\sigma^{(2)}$ for the above five stacking configurations of MoS_2-MoSSe vdW heterostructure, where we can clearly see the similarities and differences. AA and AB exhibit similar NLO response, while the primed configurations (AA', AB', and A'B) are noticeably different from the unprimed ones (AA and AB). A'B and AB' also show very similar response. Finally, the magnitude of the SHG response in AB' is generally smaller than those in the other four stacking configurations. MoS_2-MoSSe vdW heterostructures with AA and AB stacking have strong sheet SHG (~7×10^5 pm^2/V), for the element $\chi^{(2)}_{yxx}$ in a wide energy range from 1.5 eV to 3 eV. Additionally, both A'B and AB' exhibit a $\chi^{(2)}_{zxx}$ around 3.0-4.0$\times10^5$ pm^2/V in the 2-3 eV range. The MoS_2-MoSSe vdW heterostructure reveals enhancement of the SHG magnitude in several places compared to monolayer. Such enhancement is likely related to interference effect and interlayer coupling between the layers (see Figure S4 in the Supporting Information for more details). For example, for AB stacking, the $|\chi^{(2)}_{xxz}|$ was enhanced by a factor of ~2 at the peak located at 1.22 eV, $|\chi^{(2)}_{yxx}|$ was increased by a factor of 1.5-2 in the range of 1.5-3.0 eV, and $|\chi^{(2)}_{zzz}|$ was strengthened by a factor of 11 at 2.2 eV. Regarding the shift current, both AA and A'B stacking have very strong out-of-plane shift current $\sigma^{(2)}_{zxx}$ of ~25 nm μA/V^2 around 2.75-3.0 eV. These strong out-of-plane responses in chiral MoS_2-MoSSe vdW heterostructures suggest the great potential of vdW heterostructuring for ultrathin NLO and optoelectronic device applications, e.g. bulk photovoltaics based on the out-of-plane nonlinear shift current without forming *p-n* junction.

In summary, our results demonstrate that Janus 2D materials and their vdW heterostructures break the mirror symmetry of their parent 1H-MX_2 structure, thus induce the chirality. Moreover, they hold strong out-of-plane NLO responses such as SHG and shift current, which expands the material candidates for shift current photovoltaics. The large magnitude of SHG response indicates the potential of Janus MoSSe for electro-optics since the zero-field SHG tensor is directly proportional to the zero-field electro-optic tensor.[37] Additionally, replacing sulfur with selenium (or vice versa) in a Janus 2D TMD switches the chirality and thus the direction of photocurrent. Furthermore, the SHG and shift current are expected to present in other Janus 2D materials with lower symmetry. In addition, they offer great platforms to investigate other NLO responses such as the Pockels effect and four-wave mixing. Additionally, vdW heterostructures can significantly expand beyond the MoSSe bilayer or heterostructure through multilayer combinatorial stacking.

Methods

First-principles electronic structure calculations. First-principles calculations were carried out by using density functional theory (DFT)[30, 31] as implemented in the Vienna ab initio Simulation Package (VASP)[38] with the projector-augmented wave (PAW) method,[39] the exchange-correlation energy functional in the Perdew-Burke-Ernzerhof form,[32] and the plane-wave basis with an energy cutoff of 400 eV. A vacuum layer of ~20 Å was added between layers to minimize artificial image interaction between layers due to the periodic boundary condition. All the structures were fully relaxed with maximum residual force <0.005 eV/Å. For the initial relaxation and static calculation, Monkhorst-Pack $\boldsymbol{k}$-point sampling was a 10×10×1 grid.

First-principles nonlinear optical calculations. NLO susceptibility tensors, including SHG, shift current, and circular photocurrent, were calculated using an in-house developed first-principles NLO package[40] interfaced with VASP. For the NLO calculations, we used a dense k-point sampling of 70×70×1, 120 electronic bands, and total 1000 frequency grids in the energy range of [0 eV, 6 eV]. As the present NLO calculations are based on the sum-over-states approach in the first Brillouin zone, the convergence tests were performed with respect to number of electronic bands and the k-point sampling. The results are shown in Figure S5 and S6, which indicate that a k-point mesh of 70×70×1 and 120 electronic bands are enough to reach the convergence. The fundamental frequency ω in the denominator of susceptibility tensor includes a small imaginary smearing factor δ: $\omega \rightarrow \omega + i\delta$ with δ=0.05 eV in this work. We have checked the NLO tensor elements with respect to the underlying point group symmetry. Furthermore, since the thickness of 2D materials is not well-defined, *sheet* susceptibility tensors are used: $\chi^{NLO}_{sheet} = \chi^{NLO}_{bulk} * c$, where χ^{NLO}_{bulk} is the NLO susceptibility tensor calculated by using the lattice constant c along the out of plane direction.

ASSOCIATED CONTENT

Supporting Information Available

The Supporting Information is available free of charge on the ACS Publications website at http://pubs.acs.org.

Heterostructure stacking configurations and nomenclature, the effect of spin-orbit coupling and a scissor operator, comparison of SHG between monolayer Janus MoSSe and heterostructure, and convergence tests with respect to number of electronic bands and k-point sampling are available.

AUTHOR INFORMATION

Corresponding Author

* Email: feng@tamu.edu

Author Contributions

X.Q. conceived the project. A.S. performed the calculations. H.W. and X.Q. developed first-principles approach for computing nonlinear susceptibility tensor. All the authors analyzed the results and wrote the manuscript. A.S. and H.W. contributed equally to this work.

Notes

The authors declare no competing financial interests.

ACKNOWLEDGMENT

X.Q. acknowledges the support by the National Science Foundation (NSF) under award number DMR-1753054. A.S. would like to acknowledge the support by NSF through the grant DGE-1545403, Data-Enabled Discovery and Design of Energy Materials, D^3EM, and the partial support by DMR-2103842. Portions of this research were conducted with the advanced computing resources provided by Texas A&M High Performance Research Computing.

References:

(1) Lu, A. Y.; Zhu, H.; Xiao, J.; Chuu, C. P.; Han, Y.; Chiu, M. H.; Cheng, C. C.; Yang, C. W.; Wei, K. H.; Yang, Y.; Wang, Y.; Sokaras, D.; Nordlund, D.; Yang, P.; Muller, D. A.; Chou, M. Y.; Zhang, X.; Li, L. J. Janus monolayers of transition metal dichalcogenides. *Nature Nanotechnology* **2017,** 12, 744-749.

(2) Zhang, J.; Jia, S.; Kholmanov, I.; Dong, L.; Er, D.; Chen, W.; Guo, H.; Jin, Z.; Shenoy, V. B.; Shi, L.; Lou, J. Janus Monolayer Transition-Metal Dichalcogenides. *ACS Nano* **2017,** 11, 8192-8198.

(3) Ma, Y.; Kou, L.; Huang, B.; Dai, Y.; Heine, T. Two-dimensional ferroelastic topological insulators in single-layer Janus transition metal dichalcogenides MSSe(M=Mo, W). *Phys. Rev. B* **2018,** 98, 085420.

(4) Riis-Jensen, A. C.; Deilmann, T.; Olsen, T.; Thygesen, K. S. Classifying the Electronic and Optical Properties of Janus Monolayers. *ACS Nano* **2019,** 13, 13354-13364.

(5) Yagmurcukardes, M.; Sevik, C.; Peeters, F. M. Electronic, vibrational, elastic, and piezoelectric properties of monolayer Janus MoSTe phases: A first-principles study. *Physical Review B* **2019,** 100, 045415.

(6) Maghirang, A. B.; Huang, Z. Q.; Villaos, R. A. B.; Hsu, C. H.; Feng, L. Y.; Florido, E.; Lin, H.; Bansil, A.; Chuang, F. C. Predicting two-dimensional topological phases in Janus materials by substitutional doping in transition metal dichalcogenide monolayers. *npj 2D Materials and Applications* **2019,** 3, 35.

(7) Zhang, Z.; You, J.-Y.; Gu, B.; Su, G. Antiferromagnetic and Electric Polarized States in Two-Dimensional Janus Semiconductor $Fe_2Cl_3I_3$. *The Journal of Physical Chemistry C* **2020,** 124, 19219-19227.

(8) Peng, R.; Ma, Y.; Zhang, S.; Huang, B.; Dai, Y. Valley Polarization in Janus Single-Layer MoSSe via Magnetic Doping. *Journal of Physical Chemistry Letters* **2018,** 9, 3612-3617.

(9) Ma, X.; Wu, X.; Wang, H.; Wang, Y. A Janus MoSSe monolayer: A potential wide solar-spectrum water-splitting photocatalyst with a low carrier recombination rate. *Journal of Materials Chemistry A* **2018,** 6, 2295-2301.

(10) Idrees, M.; Din, H. U.; Ali, R.; Rehman, G.; Hussain, T.; Nguyen, V. C.; Ahmad, I.; Amin, B. Optoelectronic and solar cell applications of Janus monolayers and their van der Waals heterostructures. *Physical Chemistry Chemical Physics* **2019,** 21, 18612-18621.

(11) Li, F.; Wei, W.; Wang, H.; Huang, B.; Dai, Y.; Jacob, T. Intrinsic Electric Field-Induced Properties in Janus MoSSe van der Waals Structures. *Journal of Physical Chemistry Letters* **2019,** 10, 559-565.

(12) Yu, S.-B.; Zhou, M.; Zhang, D.; Chang, K. Spin Hall effect in the monolayer Janus compound MoSSe enhanced by Rashba spin-orbit coupling. *Phys. Rev. B* **2021,** 104, 1-7.

(13) Dong, L.; Lou, J.; Shenoy, V. B. Large In-Plane and Vertical Piezoelectricity in Janus Transition Metal Dichalchogenides. *ACS Nano* **2017,** 11, 8242-8248.

(14) Zhang, C.; Nie, Y.; Sanvito, S.; Du, A. First-Principles Prediction of a Room-Temperature Ferromagnetic Janus VSSe Monolayer with Piezoelectricity, Ferroelasticity, and Large Valley Polarization. *Nano Lett.* **2019,** 19, 1366–1370.

(15) Zhao, N.; Schwingenschlögl, U. Dipole-induced Ohmic contacts between monolayer Janus MoSSe and bulk metals. *npj 2D Materials and Applications* **2021,** 5, 72.

(16) Zhang, K.; Guo, Y.; Ji, Q.; Lu, A. Y.; Su, C.; Wang, H.; Puretzky, A. A.; Geohegan, D. B.; Qian, X.; Fang, S.; Kaxiras, E.; Kong, J.; Huang, S. Enhancement of van der Waals Interlayer

Coupling through Polar Janus MoSSe. *Journal of the American Chemical Society* **2020,** 142, 17499-17507.
(17) Guo, Y.; Lin, Y.; Xie, K.; Yuan, B.; Zhu, J.; Shen, P.-C.; Lu, A.-Y.; Su, C.; Shi, E.; Zhang, K.; HuangFu, C.; Xu, H.; Cai, Z.; Park, J.-H.; Ji, Q.; Wang, J.; Dai, X.; Tian, X.; Huang, S.; Dou, L.; Jiao, L.; Li, J.; Yu, Y.; Idrobo, J.-C.; Cao, T.; Palacios, T.; Kong, J. Designing artificial two-dimensional landscapes via atomic-layer substitution. *Proc. Natl. Acad. Sci.* **2021,** 118, e2106124118.
(18) Zheng, T.; Lin, Y.-C.; Yu, Y.; Valencia-Acuna, P.; Puretzky, A. A.; Torsi, R.; Liu, C.; Ivanov, I. N.; Duscher, G.; Geohegan, D. B.; Ni, Z.; Xiao, K.; Zhao, H. Excitonic Dynamics in Janus MoSSe and WSSe Monolayers. *Nano Lett.* **2021,** 21, 931–937.
(19) Wei, Y.; Xu, X.; Wang, S.; Li, W.; Jiang, Y. Second harmonic generation in Janus MoSSe a monolayer and stacked bulk with vertical asymmetry. *Physical Chemistry Chemical Physics* **2019,** 21, 21022-21029.
(20) Sipe, J.; Shkrebtii, A. Second-order optical response in semiconductors. *Physical Review B - Condensed Matter and Materials Physics* **2000,** 61, 5337-5352.
(21) Wang, H.; Qian, X. Ferroicity-driven nonlinear photocurrent switching in time-reversal invariant ferroic materials. *Sci. Adv.* **2019,** 5, eaav9743.
(22) Young, S. M.; Rappe, A. M. First principles calculation of the shift current photovoltaic effect in ferroelectrics. *Phys. Rev. Lett.* **2012,** 109, 116601.
(23) Cook, A. M.; Fregoso, B. M.; De Juan, F.; Coh, S.; Moore, J. E. Design principles for shift current photovoltaics. *Nat. Commun.* **2017,** 8, 14176.
(24) Kang, K.; Li, T.; Sohn, E.; Shan, J.; Mak, K. F. Nonlinear anomalous Hall effect in few-layer WTe 2. *Nat. Mater.* **2019,** 18, 324-328.
(25) Ma, Q.; Xu, S. Y.; Shen, H.; MacNeill, D.; Fatemi, V.; Chang, T. R.; Mier Valdivia, A. M.; Wu, S.; Du, Z.; Hsu, C. H.; Fang, S.; Gibson, Q. D.; Watanabe, K.; Taniguchi, T.; Cava, R. J.; Kaxiras, E.; Lu, H. Z.; Lin, H.; Fu, L.; Gedik, N.; Jarillo-Herrero, P. Observation of the nonlinear Hall effect under time-reversal-symmetric conditions. *Nature* **2019,** 565, 337-342.
(26) Moore, J. E.; Orenstein, J. Confinement-Induced Berry Phase and Helicity-Dependent Photocurrents. *Physical Review Letters* **2010,** 105, 026805.
(27) Sodemann, I.; Fu, L. Quantum Nonlinear Hall Effect Induced by Berry Curvature Dipole in Time-Reversal Invariant Materials. *Phys. Rev. Lett.* **2015,** 115, 216806.
(28) Wang, H.; Qian, X. Ferroelectric nonlinear anomalous Hall effect in few-layer WTe_2. *npj Computational Materials* **2019,** 5, 119.
(29) Xiao, J.; Wang, Y.; Wang, H.; Pemmaraju, C. D.; Wang, S.; Muscher, P.; Sie, E. J.; Nyby, C. M.; Devereaux, T. P.; Qian, X.; Zhang, X.; Lindenberg, A. M. Berry curvature memory through electrically driven stacking transitions. *Nature Physics* **2020,** 16, pages1028–1034.
(30) Hohenberg, P.; Kohn, W. Inhomogeneous electron gas. *Phys. Rev.* **1964,** 136, B864–B871.
(31) Kohn, W.; Sham, L. J. Self-Consistent Equations Including Exchange and Correlation Effects. *Phys. Rev.* **1965,** 140, 1133-1138.
(32) Perdew, J. P.; Burke, K.; Ernzerhof, M. Generalized gradient approximation made simple. *Phys. Rev. Lett.* **1996,** 77, 3865-3868.
(33) Dresselhaus, M. S.; Dresselhaus, G.; Jorio, A., *Group Theory: Application to the Physics of Condensed Matter*. Springer Berlin Heidelberg: 2007.
(34) Wang, H.; Qian, X. Giant Optical Second Harmonic Generation in Two-Dimensional Multiferroics. *Nano Letters* **2017,** 17, 5027-5034.

(35) Chan, Y. H.; Qiu, D. Y.; da Jornada, F. H.; Louie, S. G. Giant exciton-enhanced shift currents and direct current conduction with subbandgap photo excitations produced by many-electron interactions. *Proc. Natl. Acad. Sci.* **2021,** 118, e1906938118.
(36) Xu, S. Y.; Ma, Q.; Gao, Y.; Kogar, A.; Zong, A.; Mier Valdivia, A. M.; Dinh, T. H.; Huang, S. M.; Singh, B.; Hsu, C. H.; Chang, T. R.; Ruff, J. P. C.; Watanabe, K.; Taniguchi, T.; Lin, H.; Karapetrov, G.; Xiao, D.; Jarillo-Herrero, P.; Gedik, N. Spontaneous gyrotropic electronic order in a transition-metal dichalcogenide. *Nature* **2020,** 578, 545-549.
(37) Hughes, J. L. P.; Sipe, J. Calculation of second-order optical response in semiconductors. *Physical Review B - Condensed Matter and Materials Physics* **1996,** 53, 10751-10763.
(38) Kresse, G.; Furthmüller, J. Efficient iterative schemes for ab initio total-energy calculations using a plane-wave basis set. *Physical Review B - Condensed Matter and Materials Physics* **1996,** 54, 11169-11186.
(39) Blöchl, P. E. Projector augmented-wave method. *Physical Review B* **1994,** 50, 17953-17979.
(40) Aversa, C.; Sipe, J. E. Nonlinear optical susceptibilities of semiconductors: Results with a length-gauge analysis. *Physical Review B* **1995,** 52, 14636-14645.

Figure Captions

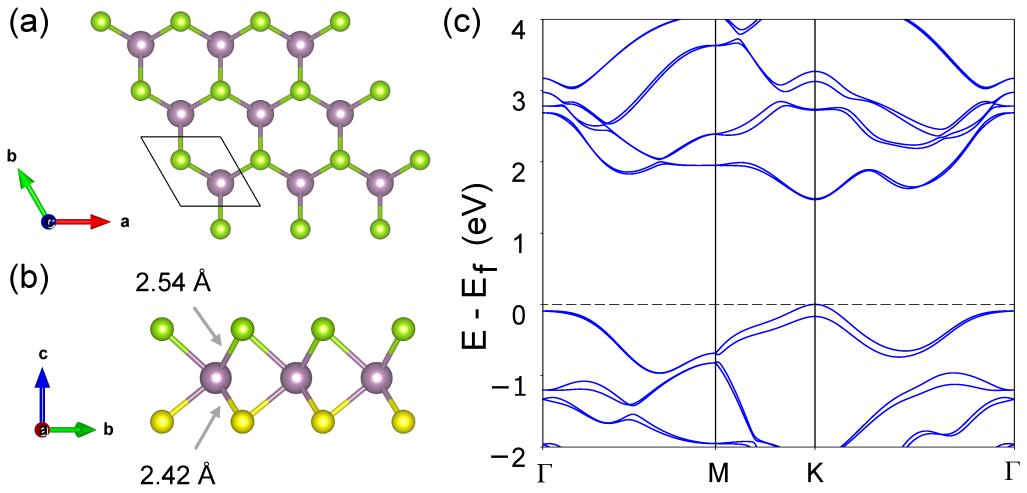

Figure 1. Janus monolayer MoSSe structure. (a) c-axis view, and (b) a-axis view. The purple atoms are molybdenum (Mo), yellow atoms are sulfur (S), and green atoms are selenium (Se). (c) Electronic band structure of monolayer Janus MoSSe. The Fermi energy was set to the valence band maximum, which is located at K.

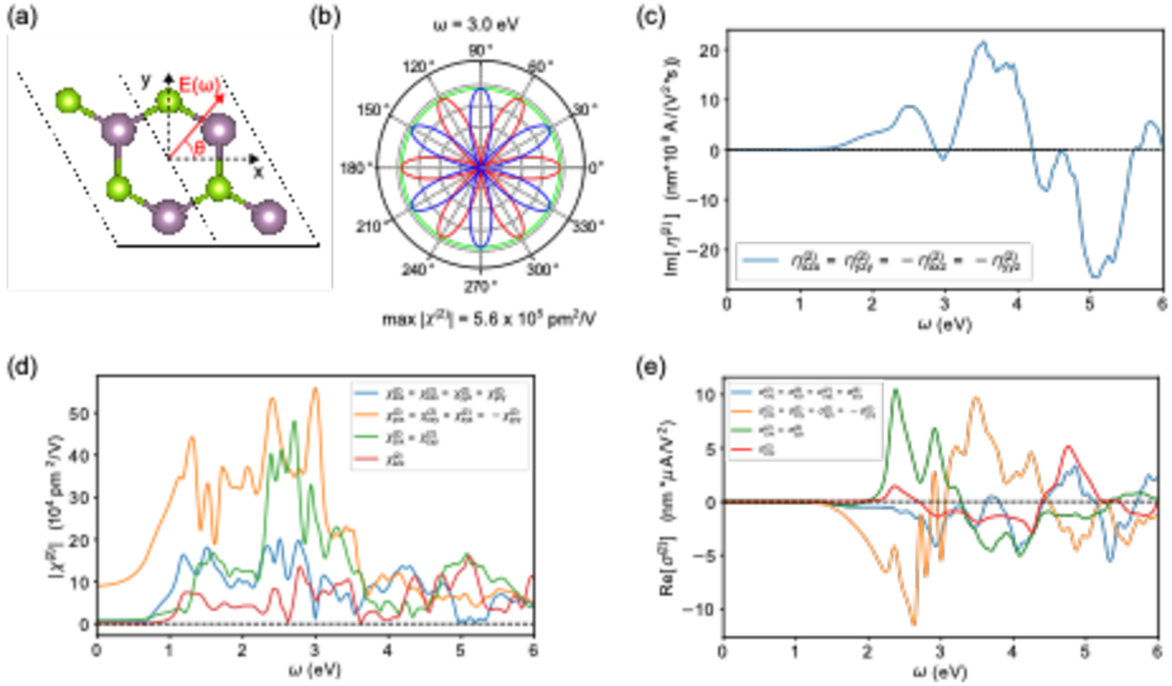

Figure 2. Nonlinear optical responses in Janus MoSSe monolayer. (a) Alignment of the electric field carried by the incoming linearly polarized light with respect to crystal lattice with the outgoing SHG polarization being parallel to the electric field. (b) SHG polarization anisotropy plot for ω=2.4 eV, indicating C_{3v} character. Red curve indicates SHG response with parallel configuration (*i.e.* $\boldsymbol{P}(2\omega) \parallel \boldsymbol{E}(\omega)$), and blue curve indicates SHG response with perpendicular configuration (*i.e.* $\boldsymbol{P}(2\omega) \perp \boldsymbol{E}(\omega)$). (c) Circular photocurrent $\eta^{(2)}_{abc}$. (d) Magnitude of second harmonic generation $|\chi^{(2)}_{abc}|$. (e) Shift current $\sigma^{(2)}_{abc}$.

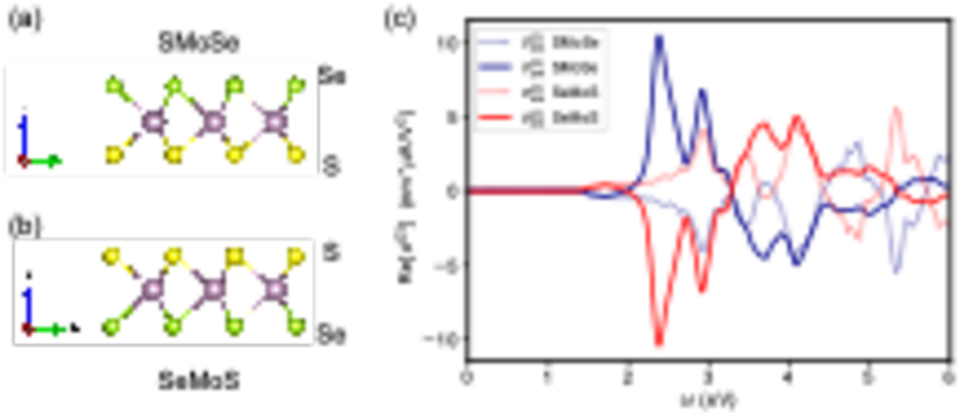

Figure 3. Out-of-plane shift current switching upon S and Se flipping. (a, b) Janus SMoSe and SeMoS with S and Se flipped on the top and bottom atomic layer. (c) Shift current susceptibility tensor element $\sigma^{(2)}_{xzx}$ and $\sigma^{(2)}_{zxx}$. The dark blue curves indicate shift current for Janus SMoSe monolayer in (a). The red curves indicated shift current for Janus SeMoS in (b). The result clearly demonstrates the current reversal upon S/Se switching in the Janus structure.

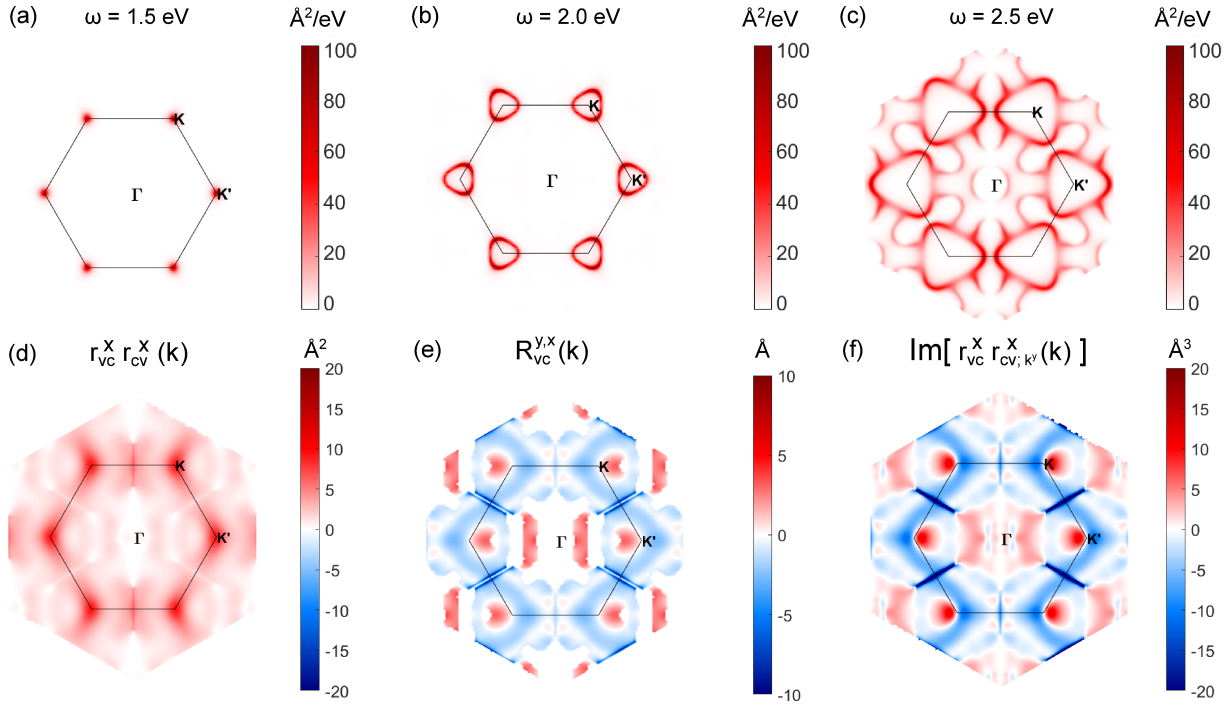

Figure 4. k-point resolved optical properties of monolayer Janus MoSSe under x-polarized light. (a-c) ***k***-resolved frequency-dependent absorption at 1.5 eV, 2 eV, and 2.5 eV, respectively. (d) ***k***-resolved dipole transition strength. (e) ***k***-resolved shift vector. (f) ***k***-resolved shift current strength.

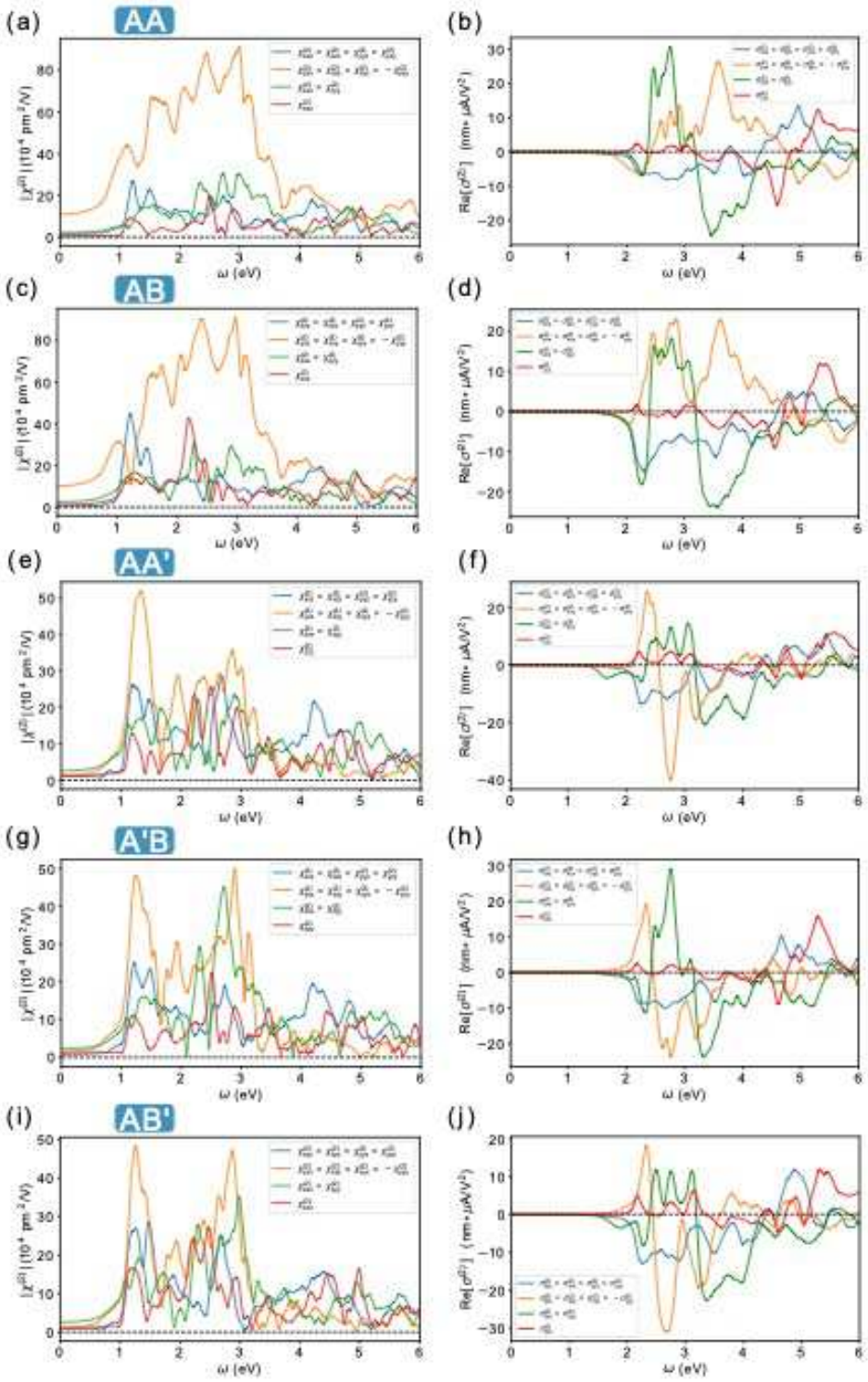

Figure 5. SHG magnitude (left column) and shift current (right column) of the five stacking configurations of the MoS_2-SMoSe heterostructure, (a-b) AA, (c-d) AB, (e-f) AA', (g-h) A'B, and (i-j) AB'.

Table of Contents Figure